

## CVD GROWTH AND HEAT TRANSFER OF CARBON NANOTUBES

Shigeo Maruyama

Department of Mechanical Engineering, The University of Tokyo,  
7-3-1 Hongo, Bunkyo-ku, Tokyo 113-8656, Japan

### ABSTRACT

Carbon nanotubes and graphene are extra-ordinal material with remarkable electrical, optical, mechanical and thermal properties. Films of vertically aligned (VA-) SWNTs and horizontally aligned (HA-) SWNTs are synthesized on quartz and crystal quartz substrates, respectively. These aligned film should inherit the remarkable properties of SWNTs. The recent progress in growth control and characterization techniques will be discussed. The CVD growth mechanism of VA-SWNTs is discussed based on the *in-situ* growth monitoring by laser absorption during CVD. For the precisely patterned growth of SWNTs, we recently propose a surface-energy-difference driven selective deposition of catalyst for localized growth of SWNTs. For a self assembled monolayer (SAM) patterned Si surface, catalyst particles deposit and SWNTs grow only on the hydrophilic regions. The proposed all-liquid-based approach possesses significant advantages in scalability and resolution over state-to-the-art techniques, which we believe can greatly advance the fabrication of nano-devices using high-quality as-grown SWNTs. The optical characterization of the VA-SWNT

film using polarized absorption, polarized Raman, and photoluminescence spectroscopy will be discussed.

The extremely high and peculiar thermal conductivity of single-walled carbon nanotubes has been explored by non-equilibrium molecular dynamics simulation approaches. The thermal properties of the vertically aligned film and composite materials are studied by several experimental techniques and Monte Carlo simulations based on molecular dynamics inputs of thermal conductivity and thermal boundary resistance. Current understanding of thermal properties of the film is discussed.

### INTRODUCTION

Geometric structure of nano-carbon material such as carbon nanotube and graphene are summarized in Fig. 1. Single-walled carbon nanotube (1) illustrated in Fig. 1 (a) is a rolled-up tube of graphene [Fig. 1 (b)], which is a single-layer graphite. Graphene has long been a theoretical concept but suddenly becomes the most popular material in physics research because

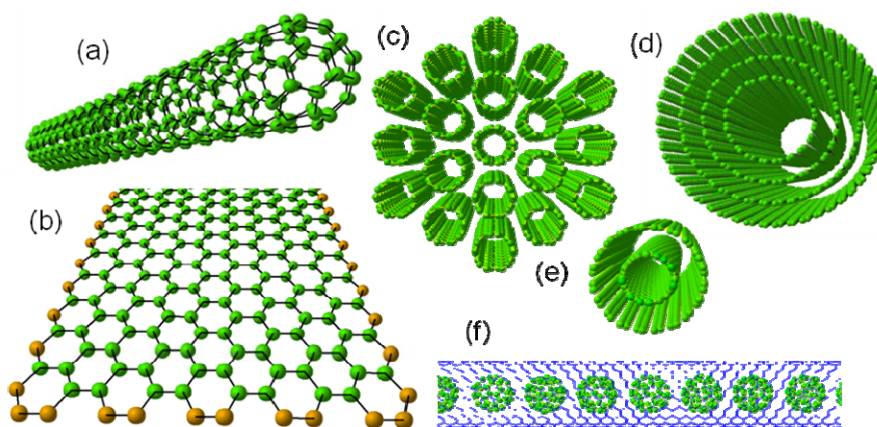


Fig. 1. Structure of nanotubes and graphene. (a) Single-walled carbon nanotube (SWNT), (b) graphene, (c) bundle of SWNTs, (d) multi-walled carbon nanotube (MWNT), (e) double-walled carbon nanotube (DWNT), (f) peapod.

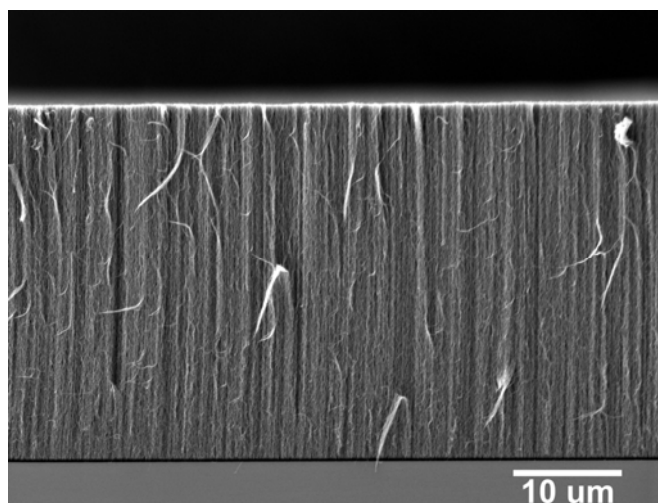


Fig. 2. VA-SWNTs grown on a quartz substrate

of the discovery of simple mechanical exfoliation technique and striking electronic mobility (2). SWNTs usually aggregate as a bundle in Fig. 1(c). Concentric carbon nanotubes as in Fig. 1(d) is called multi-walled carbon nanotubes (MWNTs). Double-walled carbon nanotubes as in Fig. 1 (d) or fullerene peapod as in Fig. 1 (e) can be synthesized as macroscopic quantity. In this paper, I will focus on SWNT which have remarkable electrical, optical, mechanical and thermal properties (3), making them not only interesting from a purely scientific perspective, but also highly desirable for development of many new applications. SWNTs have been the focus of numerous investigations in numerous fields of science and engineering. However, one challenge facing many of these studies is control over the morphology of synthesized SWNTs.

A significant development in morphology control came when the alcohol catalytic CVD technique (4) was combined with a simple dip-coat preparation of catalytic metal particles. The result was vertically aligned (VA-)SWNT films (5) synthesized on quartz substrates as shown in Fig 2. These films can exceed 30  $\mu\text{m}$  in thickness, and consist of thin, vertically aligned SWNT bundles. Many other methods were developed soon after, such as water-assisted (6), oxygen-assisted (7), microwave plasma (8), and molecular beam (9) synthesis. Among these methods, the ACCVD method is arguably the simplest, and unique in that the catalyst can be applied by various methods such as the original dip-coating method (10) and combinatorial sputtering deposition (11, 12). In this paper, we use a solution-based dip-coating method (10) that has been shown to produce monodisperse nanoparticles (13) with diameters of approximately 2 nm. Some advantages of this wet approach include deposition of a very small amount of metal catalyst, as well as excellent potential for low-cost scalability. We also extend this wet process to tailor the key structural parameters of the SWNTs array, including diameter, length, and growth location of the SWNTs. Specifically, the patterned

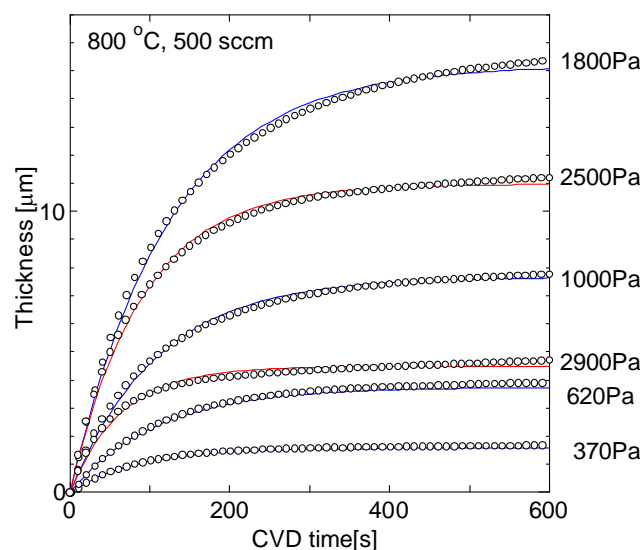


Fig. 3. *In-situ* measurement of film thickness of vertically aligned SWNTs by laser absorption during CVD.

growth of SWNTs by patterning of  $\text{SiO}_2$  layer (14) and by patterning self-assembled monolayer (SAM) film (15). The first approach (14) is the conventional concept of using  $\text{SiO}_2$  patterned Si substrates to selectively grow 3D carbon nanotube structures. High-quality VA-SWNT patterns can be easily obtained by this protocol. Apart from the sintering of catalyst into Si at high temperature, the difference in surface wettability between Si and  $\text{SiO}_2$  also plays an important role in this selective growth, which leads us to a novel method of patterning the growth on chemically modified surfaces. The latter approach (15) is based on the substrate wettability, which is found to be critical for the yield of SWNTs. On an OH-terminated hydrophilic Si/ $\text{SiO}_2$  surface, the growth can be promoted by 10 times, but can be completely suppressed on a  $\text{CH}_3$ -terminated hydrophobic surface. Selective surface modification is utilized to localize the growth of SWNTs. The proposed technique has advantages in improved simplicity and potentially better resolution compared to conventional lithography. Related to our previous finding that no-flow ACCVD is suited for growth of longer VA-SWNTs (16), some updated understanding of the decomposition of ethanol in ACCVD is also presented (17).

## CVD GENERATION TECHNIQUE

The SWNT arrays used in this study were synthesized by the ACCVD method (4), where typically cobalt and molybdenum nanoparticles were loaded onto a silicon or quartz substrate by a liquid-based dip-coat method (10). The details and procedures have been described in previous reports (5, 18, 19, 20, 21) but essentially involve two dip-coating steps—once in a Mo solution, and once in a Co solution— followed by low-pressure alcohol CVD at 700–800  $^\circ\text{C}$ . Each dip-coat step is followed by calcinations in air for 5 min at 500  $^\circ\text{C}$ . Synthesis

by this method has been shown to be a root-growth process (22), with catalyst nanoparticles remaining on the substrate surface and SWNTs growing perpendicular to the substrate. The growth process has been investigated using an *in situ* optical absorbance measurement (18), which shows the growth rate decays exponentially from an initial maximum. The resulting VA-SWNT arrays typically have a thickness of 10-30  $\mu\text{m}$ , and consist of small bundles of ten or fewer SWNTs (23). The diameters range from 0.8 to 3.0 nm, with an average diameter of 2.0 nm (23). Our standard synthesis conditions are 800  $^{\circ}\text{C}$  and 1.4 kPa (10 Torr) of ethanol at a flow rate of 450 sccm. Standard catalyst concentrations are 0.01 wt% of both Mo and Co. The catalyst nanoparticles are reduced under 40 kPa (300 Torr) of 3%  $\text{H}_2$  (Ar balance) during heating of the CVD chamber, but the Ar/ $\text{H}_2$  flow is stopped prior to the introduction of ethanol.

### GROWTH DYNAMICS

The growth condition and growth mechanism of VA-SWNTs is explored based on the *in-situ* growth monitoring by laser absorption during CVD (18, 20). As shown in Fig. 3, film thickness  $L$  of VA-SWNTs film at various temperature, flow-rate, and pressure can be well fit by an empirical equation:

$$L = \gamma_0 \tau (1 - \exp(-t/\tau))$$

where  $\gamma_0$  and  $\tau$  are initial growth rate and growth decay time, respectively. The initial growth rate  $\gamma_0$  is linearly proportional to pressure up to the critical pressure which is determined by temperature (20). This result indicates the first order reaction below the critical pressure.

Recently developed removal and transfer technique of this film (24) enabled a direct TEM observation of free-standing vertically aligned SWNTs along the alignment direction. It was revealed that the film is comprised primarily of small SWNT bundles, typically containing 3-8 SWNTs (23). This minimum bundling structure is ideal for various optical characterizations such as resonant Raman (25) and possible production of homogeneous composite materials (26). Optical characterization of such a film using polarized absorption, polarized Raman, and photoluminescence spectroscopy will be discussed. Laser-excitation of a vertically aligned film from top means that each nanotube is excited perpendicular to its axis. Because of this predominant perpendicular excitation, interesting cross-polarized absorption (27) and interesting and practically important Raman features as shown in Fig. 3 are observed (28). Polarization-dependent resonance Raman spectra of VA-SWNT were measured such that the polarization of the scattered light was selected either parallel or perpendicular to that of the incident light. For the parallel configuration, radial breathing mode (RBM) peaks exhibited two different polarization dependencies. One group (dominated by a peak at 203  $\text{cm}^{-1}$ ) had a maximum scattering intensity for incident light parallel to the alignment direction, whereas the

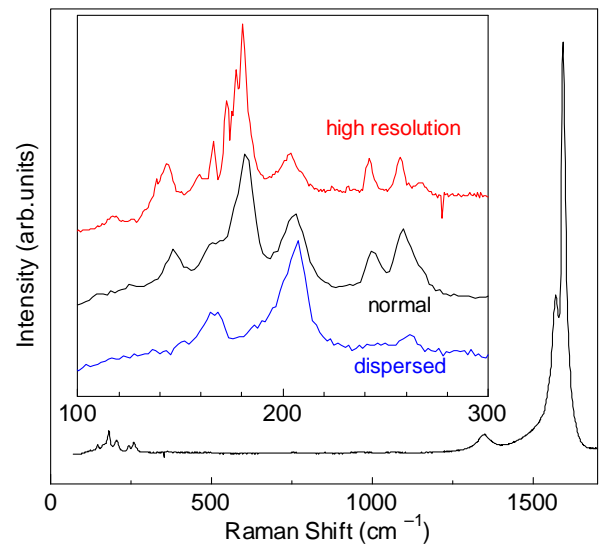


Fig. 4 Anomalous radial breathing mode of Raman scatterings excited from the top of a VA-SWNTs film. Raman spectra taken from the top of a VA-SWNT array. Inset shows the RBM region with high-resolution (topmost) and with normal resolution before (middle) and after (lower) dispersion in  $\text{D}_2\text{O}$ .

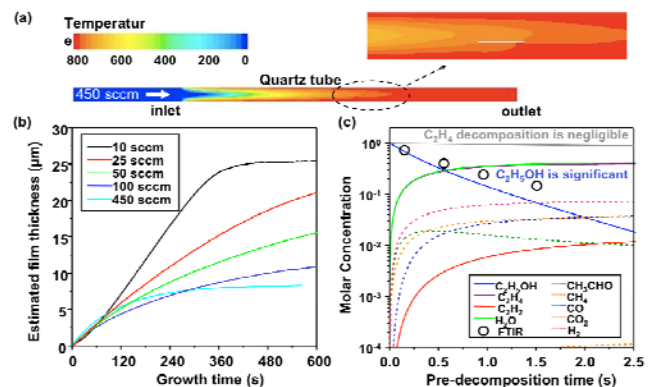


Fig. 5 (a) Temperature distribution inside the quartz tube during CVD. (b) Growth curves at 800  $^{\circ}\text{C}$  for different ethanol flow rates show a change for slow flow rates. (c) Ethanol decomposition curves calculated by CHEMKIN, and experimentally measured ethanol concentrations (circles) by FT-IR spectroscopy.

other group (dominated by a peak at 181  $\text{cm}^{-1}$ ) had maximum intensity for excitation perpendicular to the alignment direction. This anomaly has been attributed to resonance with non-vertical transitions due to perpendicularly polarized excitation before. Decomposing the Raman spectra and comparing to theoretical expectations for the two different configurations revealed that the 203  $\text{cm}^{-1}$  group peaks behave as expected for parallel-polarized dipole excitation, whereas the 181  $\text{cm}^{-1}$  group peaks deviate significantly from the prediction assuming perpendicularly polarized excitation. Furthermore,

after correcting the spectra for laser-induced heating effects, the  $181\text{ cm}^{-1}$  group peak intensities were found to be essentially independent of polarization angle. The sound interpretation of these results is that the RBM anomaly is due to the parallel excitation of ‘stray’ SWNTs suspended within the vertically aligned array.

### GAS PHASE THERMAL DECOMPOSITION

The non-flow CVD (16) turned out to be very efficient, resulting a thicker film up to  $100\ \mu\text{m}$ . The growth curve is obviously different probably because of the contribution of small amount of acetylene thermally decomposed from ethanol (17). The carbon conversion rate from ethanol to VA-SWNTs can be as high as 40 %. Hence, isotopically modified ethanol can be employed to study the growth process (22). The detailed chemical reaction process in gas-phase and on metal catalysts will be discussed based on CVD results using isotope labeled ethanol and acetylene as carbon source.

We have previously investigated the influence of CVD temperature and pressure on the synthesis of VA-SWNTs by ACCVD (20). However, since ethanol thermally decomposes at typical growth temperatures (17), the actual catalyst environment can be significantly affected by the gas flow rate, even when the furnace temperature is unchanged. Fig. 5a shows the temperature profile based on a numerical calculation using the FLUENT software package for an ethanol flow rate of 450 sccm through a 60 cm furnace maintained at a temperature of  $800\ ^\circ\text{C}$ . The dashed oval indicates the position of the substrate, and is found to be approximately  $20\ ^\circ\text{C}$  cooler than the furnace temperature. Thermal decomposition of ethanol under these conditions was also calculated, and the concentrations of ethanol and various chemical species produced by its thermal decomposition are shown in Fig. 5c. Under these conditions, ethanol almost completely decomposes in 2.5 seconds. The residence time in the chamber, however, is only 0.1 s, thus the ethanol concentration near the catalyst should be more than 90%. In the case of a slower flow rate the gas would be heated to the furnace temperature by the time it arrives at the substrate (due to the shorter entrance length), thus slightly increasing the local temperature at the catalyst. Much more importantly, a slower flow would increase the residence time of ethanol in the heated region. As a result, a more significant portion of the ethanol would have thermally decomposed before reaching the catalyst. This is evidenced experimentally by the growth curves presented in Fig. 5b, which correspond to different ethanol flow rates under otherwise identical conditions. As the flow rate decreases the catalyst lifetime increases significantly, enhancing SWNT growth. This is likely due to an increase in the production of  $\text{C}_2\text{H}_4$  and  $\text{H}_2\text{O}$ . In most cases the general growth behavior is typical exponential decay (20), but when the flow rate is very slow (i.e.,  $<25\text{ sccm}$ ) the growth process changes significantly, as shown by the topmost black curve in Fig. 5b. In this case the growth rate is nearly constant for approximately three minutes and then suddenly stops. This catalytic sudden-death has been

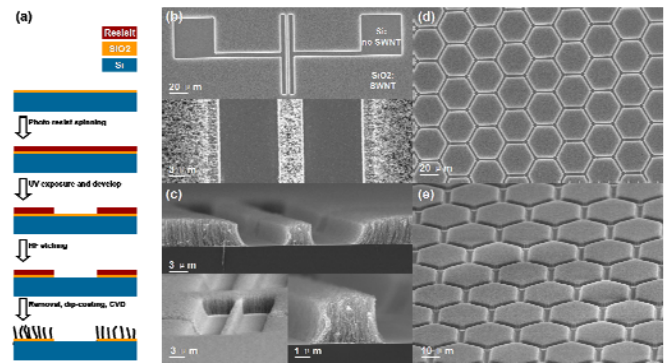


Fig. 6: (a) Schematic showing the substrate fabrication and selective growth; (b) Top and (c) side view SEM images of an electrode-shaped pattern, where SWNTs only grew in the  $\text{SiO}_2$  regions. (d) Top and (e) side view images of hexagon-shaped patterns. The growth behavior of SWNTs at the edges is slightly different from in the center of a vertically aligned forest.

reported elsewhere (29-31), but the mechanism still remains as an open question in this field.

### PATTERNED GROWTH ( $\text{SiO}_2$ –BASED PATTERN)

SWNT arrays were grown on  $\text{SiO}_2$  patterned Si substrates using ethanol as a carbon source and Co as the catalyst. A 50 nm thick  $\text{SiO}_2$  layer was patterned on a Si wafer using standard UV lithography combined with HF etching. A schematic showing the fabrication process is shown in Fig. 6a. The catalyst was loaded onto the substrate by the previously reported dip-coating process. The substrate was submerged into the dip-coating solution (0.1% wt. cobalt acetate in ethanol), soaked for 3 min, and withdrawn slowly at 4 cm/min. The substrate was then baked in air at  $400\ ^\circ\text{C}$  for 5 min before CVD. Only cobalt acetate was used here as the catalyst precursor because we recently found VA-SWNT arrays can still be obtained when Mo is absent, as long as the parameters are well optimized. ACCVD was performed at  $700\text{--}800\ ^\circ\text{C}$  with an ethanol flow of 450 sccm at a pressure of 1.3 kPa.

Figure 6b shows typical top-view SEM images of an electrode-shaped SWNT pattern (14). It is clear that SWNTs grow only in regions where an oxide layer is present. No growth was observed in areas where the oxide layer had been etched by HF. The SWNT structures can form lines, hexagons (Fig. 6d) or other shapes depending on the pre-designed pattern. The resolution of this method is limited by the ability of obtaining oxide area on a Si wafer. In this experiment, a linewidth of several micrometers was achieved using UV lithography. If other higher resolution techniques (e.g. electron-beam lithography, scanning probe oxidation) were used, finer SWNT structures may be obtained. The convenience in this approach is that the regions where SWNTs grow can be well controlled by pre-fabrication. Dip-coating was performed on

the entire substrate and no further processing (e.g., lift-off) was needed.

The cross-sectional view of a pattern (Fig. 6c) confirmed the alignment of the obtained SWNTs. However, SWNTs can also grow into random networks if the catalyst density is significantly decreased. Both edges of a line pattern always exhibit transition regions, where the SWNTs are not perfectly perpendicular to the substrate. Apart from these few micrometers, however, the alignment is essentially the same as in VA-SWNT arrays. The formation of such transition regions is very likely due to the different wetting behavior of liquid at the edge. Further study is needed to understand and control this phenomenon.

### PATTERNED GROWTH (SAM-BASED PATTERN)

The effects of surface chemistry on the yield of SWNTs suggest the ability to control the growth position, which is critical to constructing 3-D vertically aligned SWNT structures or 2D SWNT patterns on a substrate (15). To selectively suppress growth created the opposite effect of plasma treatment, i.e. increased the hydrophobicity of the surface, by forming a SAM of octadecyltrichlorosilane (OTS) on the substrate surface (32). The terminating  $\text{CH}_3$  group makes the surface super-hydrophobic, increasing the contact angle of water from nearly 0 (for OH-terminated) to approximately  $110^\circ$ . After dip-coating and CVD, almost no carbon structures were found on the substrate. The effects of these surface treatments are compared in Fig. 7, which shows that an OH-terminated surface significantly boosted the array height, while a  $\text{CH}_3$ -terminated surface effectively prevented SWNT synthesis.

The appeal of using an SAM lies in not only the easy fabrication and drastic change of surface energy (by only one layer of molecules), but also the reversibility of the SAM process. For example, deep UV light (here 254 nm) is known to be able to remove the SAM effectively. The exposed surface can retrieve its hydrophilicity (water contact angle returns to almost  $0^\circ$ ) and SWNTs can efficiently grow on it. Therefore, by combining with a masking technique, silicon surfaces with sharp hydrophilic/hydrophobic patterns can be easily obtained. A schematic of this process is presented in Fig 8a. Line patterned SWNTs obtained after dip-coating and CVD are shown in Fig. 8b. Regions exposed to UV radiation after SAM formation clearly produced SWNTs with high density. On the other hand, no SWNTs grew in the masked areas, as no catalyst was deposited due to the high hydrophobicity of the surface. Importantly, the fabrication of patterned catalyst through this all-liquid route is both simpler and more efficient than conventional photolithography, as developing and removal of photo-resist is bypassed. Compared to the post-pattern techniques, which normally introduce some irreversible destruction and contamination (e.g. pre-dispersion with surfactant) to the SWNTs, these high-quality as-grown SWNTs are expected to give better performances in device applications.

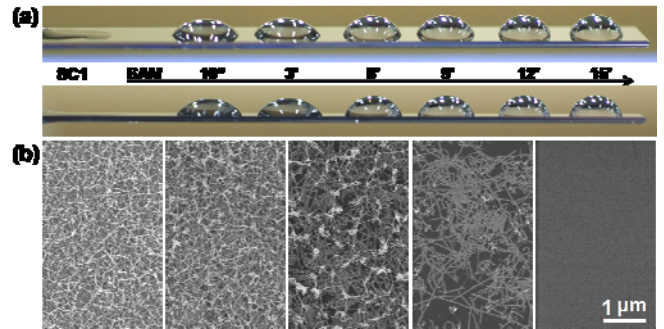


Fig. 7 (a) Various contact angles of water droplets on hydrophilic surface terminated by OH after standard cleaning 1 (SC1) and hydrophobic surface functionalized by OTS monolayer with different SAM converge; (b) SEM images of SWNTs grown on substrate shown in (a) after catalyst dip-coating.

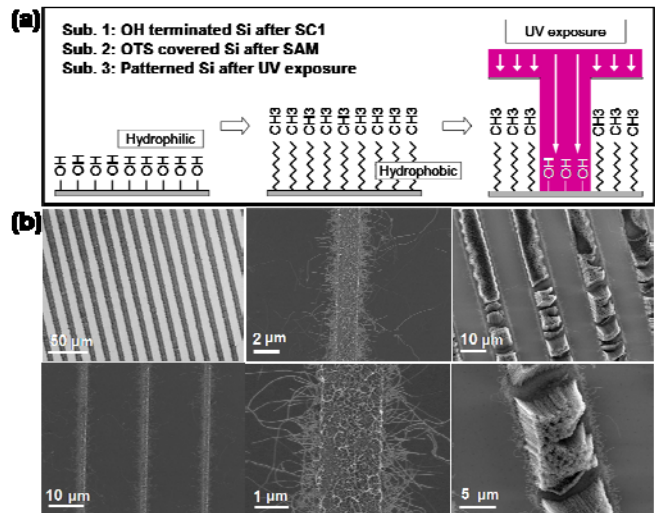


Fig. 8 (a) Schematics describing the fabrication procedure of hydrophilic/hydrophobic patterns using a selective removal of OTS SAM by UV exposure; (b) SEM images of random and vertically aligned SWNT line-shape patterns.

### HEAT TRANSFER OF NANOSCALE MATERIALS

Among 3 modes of general heat transfer, i.e. heat conduction, convective heat transfer, and radiative heat transfer, only heat conduction is the concern in nanoscale heat transfer problems. It is straightforward to disregard the effect of convective heat transfer compared to heat-conduction. Characteristic non-dimensional numbers such as Reynolds number  $Re = \frac{Ud}{\nu}$  or Grashof number  $Gr = \frac{g\beta\Delta Td^3}{\nu^2}$  are very small because of characteristic size  $d$ . Furthermore, heat

flux in convective heat transfer  $q_{conv} = h(T_w - T_\infty) = h\Delta T$  reduces with the temperature difference. On the other hand, heat flux in heat conduction  $q_{cond} = -\lambda \frac{\partial T}{\partial x}$  keeps its importance because of the temperature gradient. The ratio of heat fluxes of convective heat transfer and heat conduction can be described as Nusselt number  $Nu = \frac{hd}{\lambda}$ , which will be infinitesimal. The Biot number, the ratio of convection and heat-conduction of material,  $Bi = \frac{hd}{\lambda_s}$  is also infinitesimal for nanoscale  $d$ . The non-steady heat conduction term  $\rho c_p V \frac{\partial T}{\partial t} \approx \rho c_p d^3 \frac{\partial T}{\partial t}$  becomes small compared with heat conduction term  $-A\lambda \frac{\partial T}{\partial x} \approx -d^2 \lambda \frac{\partial T}{\partial x}$ . Being Fourier number  $Fo = \frac{\alpha t}{d^2}$  infinitely large as proportion to  $d^2$ , most of problems can be handled as steady state even with very fast heating.

The radiative heat flux from a nano-material surrounded by environment can be characterized by  $q_{rad} = \varepsilon_s \sigma (T_w^4 - T_\infty^4)$ , where the environment temperature is  $T_\infty$ . Because the length-scale between the nano-material and surrounding is usually small, the temperature difference is also small due to heat-conduction contribution. Hence, the effect of radiative heat flux is generally small compared with heat-conduction.

The practical heat transfer problem of nanoscale material is, hence, heat conduction. However, we need to raise 2 new problems intrinsic to nanoscale. The first problem is that thermal conductivity of nanomaterial may be quite different from ordinary material. We need to seriously consider phonon dynamics for heat conduction problem even at room temperature, because characteristic size of nanomaterial can be comparable or smaller than phonon mean free path and/or because discrete nature of phonon density of states manifests. The former problem is already well discussed with micron-size thin films, but the latter is unique for a nanomaterial. This gives a complexity of the analysis and at the same time a unique opportunity of the application of such nano-materials. Thermal conductivity of fluid in nanoscale area is also affected by molecular nature of fluid.

The second problem is the manifest of thermal boundary resistance  $R_T$  between materials. With the same formula as macroscopic contact resistance, thermal boundary resistance is defined as  $q = \frac{1}{R_T} (T_{s \rightarrow} - T_{s \leftarrow}) = K_T (T_{s \rightarrow} - T_{s \leftarrow})$ , where temperature jump difference left and right materials ( $T_{s \rightarrow} - T_{s \leftarrow}$ ) is assumed to be the heat flux  $q$  across the boundary surface. Here, we often use thermal boundary conductance  $K_T = 1/R_T$ . This concept has been well known as Kapitza resistance between solid materials but is also very

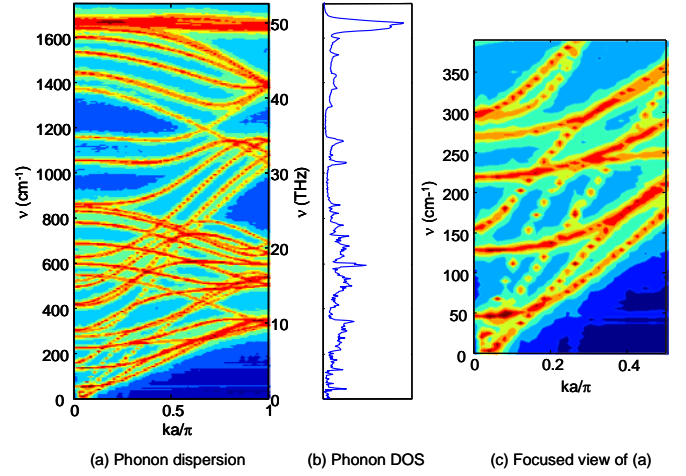


Fig. 9 (a) Discrete phonon dispersion relations and (b) phonon density of states (DOS) of a 25 nm-long (5, 5) SWNT. The dispersion relations were obtained by computing the phonon energy spectral density from MD simulations. Wavevector  $k$ -space is normalized by the Brillouin-zone width  $\pi/a$ . In the current case with an armchair SWNT,  $a = \sqrt{3}a_{c-c}$ , where  $a_{c-c}$  is the interatomic distance. The focused view (c) shows the phonon dispersion in the low frequency region for clarity.

important between solid-fluid boundary (33). Because the characteristic length scale  $L_R = \lambda R_T$  is order of 10 nm for a typical solid-fluid system (33), this resistance is simply negligible in macroscopic system but is the most important parameter for evaluation of thermal conductivity of nano-composite materials.

Peculiar nature of thermal conductivity of carbon nanotubes and several thermal boundary resistance problem will be discussed.

## DIFFUSIVE-BALLISTIC HEAT CONDUCTION

SWNTs are expected to possess high thermal conductivity due to their strong carbon bonds and the quasi-one-dimensional structure (34). On considering the actual applications, one of the essential tasks is to characterize the thermal properties not only for thermal devices but also for electrical devices since they determine the affordable amount of electrical current through the system. Following the thermal conductivity measurements of SWNTs in forms of mats and bundles (35), with advances in SWNT synthesis and MEMS techniques, thermal conductivity (or thermal conductance) measurements of individual carbon nanotubes have been reported not only for multi-walled carbon nanotubes (36, 37), but also for SWNTs (38, 39). However, thermal property measurements of SWNTs in experiments are still extremely challenging as there are potential uncertainties residing in the technicality for instance related to the contact resistances between thermal reservoirs

and an SWNT. Uncertainties also arise in the identification of an isolated SWNT and its diameters. Therefore, reliable theories and numerical simulations are greatly demanded especially to investigate detailed heat conduction characteristics that are not yet accessible in experiments. One of such heat conduction characteristics with a practical importance is the size effect on thermal conductivity. In general, the size-dependence of thermal conductivity appears when the system characteristic length is smaller or comparable to the phonon mean free path (40). For SWNTs, due to the expected long phonon mean free path, the regime of the length effect stretches beyond the realistic length in many applications. The length effect has been demonstrated using molecular dynamics (MD) simulations (41, 42) and the power-law divergence was discussed with analogy to the low-dimensional models, where the *hydrodynamic effect* gives rise to the long-time heat flux correlation (43). More recently, the length dependence of thermal conductivity was investigated up to fully diffusive phonon transport regime using a kinetic approach (44), where the divergence due to long wave-length phonons was shown to disappear with presence of the second order (or higher) 3-phonon scattering processes. The issue of the transition from the pure ballistic to diffusive-ballistic phonon transport has been discussed by modeling the energy transmission based on the ratio of the overall average phonon mean free path to  $L$  (45).

The carbon-carbon interactions were modeled using Brenner potential (46) in a simplified form (47) where the total potential energy of the system is expressed as,

$$E = \sum_i \sum_{j(i<j)} [V_R(r_{ij}) - B_{ij}^* V_A(r_{ij})] \quad (1)$$

Here,  $V_R(r)$  and  $V_A(r)$  are repulsive and attractive force terms, which take a Morse type form with a certain cut-off function.  $B_{ij}^*$  represents the effect of the bonding order parameters. As for the potential parameters, we employ the set that has been shown to reproduce the linear phonon transport properties with sufficient accuracy. The velocity Verlet method was adopted to integrate the equation of motion with the time step of 0.5 fs. The application of classical approach is encouraged by the expected dominant contribution on the heat conduction from phonons compared with that from electrons (48, 49).

On simulating diffusive-ballistic phonon transport using MD simulations, linear transport properties (group velocity) need to be reproduced with sufficient accuracy. This needs to be satisfied for phonons with a wide range of frequencies as their ballistic transport becomes important for short SWNTs at room temperature. Linear phonon transport properties can be visualized by the dispersion relations, which can be computed from MD simulations by taking the two-dimensional Fourier spectra of the time history of the one-dimensional velocity field along an SWNT (50). In Fig. 9, the spectra of a 25 nm (5, 5)-SWNT at 300 K with the periodic boundary condition is presented (50) together with corresponding phonon density of states (DOS). The phonon energy spectral density is computed as Ref. (51),

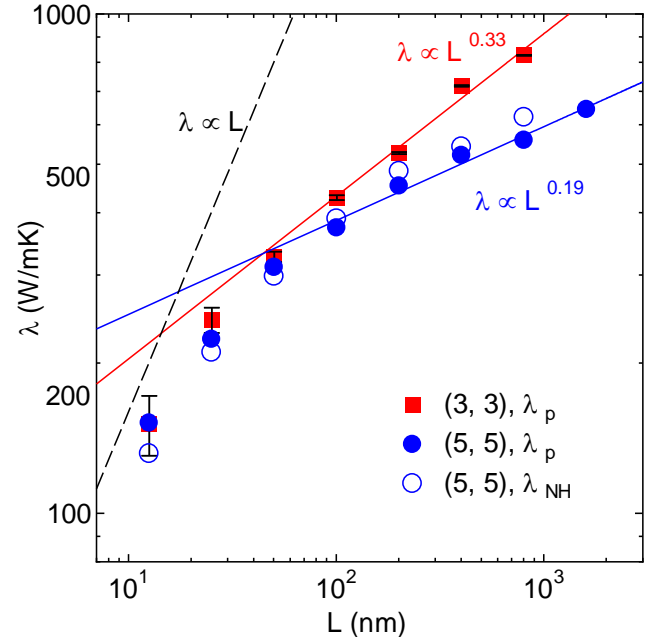


Fig. 10 Length dependences of SWNT thermal conductivity for two different diameters.  $\lambda_p$  and  $\lambda_{NH}$  denote the values obtained by using phantom and Nose-Hoover thermostats, respectively. The error bars are based on the fitting residuals in the thermal conductivity calculations. The residuals were largest in the case of (3, 3) SWNTs. The thermal conductivity profiles of (3, 3) and (5, 5) SWNTs for  $L > 100$  nm were fitted to power laws. The dashed line shows  $\lambda \propto L$  with an arbitrary slope.

$$\Phi(\omega, k) = \frac{m}{2} \sum_p \sum_\alpha \left[ \frac{1}{N} \sum_{n=0}^{N-1} \left[ e^{i\frac{n}{N}k} \int v_\alpha(n, t) e^{-i\omega t} dt \right] \right]^2 \quad (2)$$

$(\alpha = r, \phi, z)$

where  $N$  is the number of atoms in the longitudinal ( $z$ ) direction (the number of unit cells in the nanotube).  $p$  and  $m$  are the number of atoms per unit cell and the mass of a carbon atom, respectively. The data are discrete due to the finite length of the nanotube and the broadening of the spectral peaks indicates the thermal phonon scattering. The overall feature of dispersion relations obtained from MD simulations agrees with the reported theoretical models (52, 53), especially well with the mechanical model of Mahan and Jeon (53). The phonon DOS  $g(\omega)$  can be calculated from  $g(\omega)\hbar\omega\eta(\omega) = \sum_k \Phi(\omega, k)$ , where the equilibrium phonon distribution  $\eta(\omega) = k_B T / \hbar\omega$  at the classical limit.

Note, for SWNTs, as the number of phonon branches is determined by the number of atoms in a unit-cell, even armchair (or zigzag) SWNTs whose unit-cell contains fewer atoms than the other structures with similar diameters, the

dispersion relation depicts diverse phonon branches, as seen in Fig. 9 for a (5, 5) SWNT. There are optical phonon modes with small circumferential wave number and low frequency that have similar dispersion characteristics and heat capacity to the acoustic ones, especially in the intermediate wavevector ( $k$ ) regime. Although, acoustic modes may still possess the longest mean free path, the contribution of these optical modes is expected to become important when their mean free paths are comparable to  $L$ .

As shown in Fig. 10, the diffusive-ballistic heat conduction of finite-length single-walled carbon nanotubes has been studied (50). Thermal conductivity  $\lambda$  of an SWNT can be measured with non-equilibrium MD simulations. After reaching an isothermal state at 300 K with the auxiliary velocity scaling control, the temperature controlled layers on both ends of the SWNT were activated to apply a temperature difference of 20 K. Eventually the system converges to a quasi-stationary state with linear temperature gradient. By calculating the heat flux along the SWNT from the energy budgets of the thermostats,  $\lambda$  was calculated through the Fourier's law. The cross-sectional area  $A$  of an SWNT was defined using the ring of van der Waals thickness  $\pi b d$ , where  $b=0.34$  nm. The length dependence of thermal conductivity shown in Fig. 10 is quantified for a range of nanotube lengths up to 1.6  $\mu\text{m}$  at room temperature (50). A gradual transition from nearly pure ballistic to diffusive-ballistic heat conduction was identified from the thermal conductivity profile. In the diffusive-ballistic regime, the profile exhibits power-law length dependence and does not converge even for a tube length of 1.6  $\mu\text{m}$  as shown in Fig. 10 (50). We also present a theoretical scheme that seamlessly handles the crossover from fully ballistic to diffusive thermal transport regimes (54). At room temperature, the micrometer-length nanotubes belong to the intermediate regime in which ballistic and diffusive phonons coexist, and the thermal conductance exhibits anomalous nonlinear tube-length dependence due to this coexistence. This result is in excellent agreement with molecular-dynamics simulation results showing the nonlinear thermal conductance. Furthermore, recent experimental results show the length dependent thermal conductivity of carbon nanotubes and suggest the diffusive-ballistic regime in room temperature (55).

From the theoretical view, the diffusive-ballistic phonon transport regime covers a wide range of nanotube-lengths in actual applications due to the extraordinary long phonon mean free path at room temperature. This gives rise to various unique stationary and non-stationary heat conduction characteristics (51, 56).

### THERMAL BOUNDARY RESISTANCE

While these quasi-ballistic thermal transport properties encourages SWNTs for thermal/electrical device applications, on considering integrated systems in practical situations, interfacial heat transfer between nanotubes and surrounding materials becomes important. In many practical devices, the applicable heat load to the system is determined by the thermal

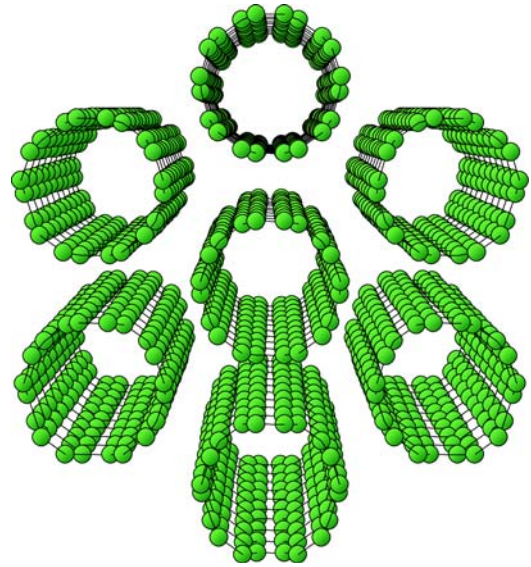


Fig. 11. Initial condition of SWNT bundle simulation.

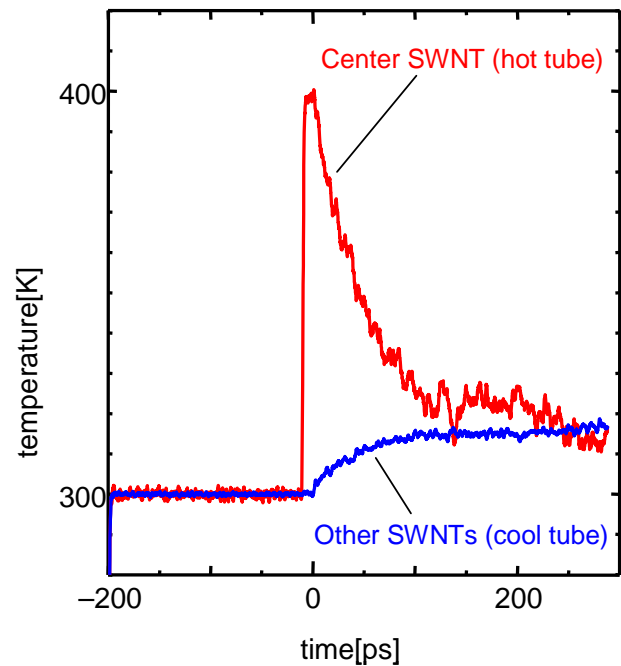


Fig. 12. Time histories of the temperature of hot (central) SWNT and cold (surrounding) SWNTs.

boundary conductance between SWNT and surrounding heat sinks/sources rather than the thermal conductance through a carbon nanotube itself. One representative case is the carbon nanotube composite, which has been explored widely aiming at bulk applications (57-60). The important role of thermal boundary conductance has been discussed (60). On the other hand, we have been developing an off-lattice Monte-Carlo simulation to study non-isotropic heat conduction in aligned or

random carbon nanotube-polymer nanocomposites or carbon nanotubes in fluids (61-64). The effective thermal conductivity of this composite material is almost fully controlled by the thermal boundary conductance between carbon nanotubes and matrix material (61-64).

We have used molecular dynamics simulations for the characterization of thermal boundary resistance in several practical situations (65, 66). As an example, thermal boundary resistance between SWNTs is briefly discussed below (65). As the initial condition, 7 SWNTs with the length of 2.51 nm were placed in a 2.51×6.0×6.0 nm simulation cell as in Fig. 11. Each SWNT was a (5, 5) armchair tube with 0.693 nm in diameter. At the beginning of the computation, the whole system was kept at 300 K for 100 ps. The inter-tube distance at equilibrium distance approximately corresponds to  $\sigma$ . Then, the temperature of only the central SWNT was suddenly increased to 400 K using the velocity scaling method for 10 ps. After that, all the temperature controls were turned off.

Figure 12 shows a time history of the temperature of the hot (central) tube and cold (surrounding) tubes. Here, the heat transfer from the central tube to surrounding tubes is clearly observed. In order to examine this heat transfer, temperature difference of central and surrounding tubes is fit to an exponential function as in Fig. 13;

$$T_{hot} - T_{cold} = T_0 \exp\left(-\frac{t}{\tau}\right), \quad (3)$$

where  $T_0 = 99.58$  K,  $\tau = 48.7$  ps.

The non-stationary heat transfer problem can be simplified if the intra-tube resistance to heat transfer is small compared to the inter-tube thermal boundary conductance. This is the case in the current problem as the nanoscale ‘‘Biot’’ number is very small with the extremely small characteristic length of an SWNT. Then the lumped capacity method in Eq. (4) can be adopted,

$$T_{hot} - T_{cold} = T_0 \exp\left[-\left(\frac{1}{\rho_{hot}c_{hot}V_{hot}} + \frac{1}{\rho_{cold}c_{cold}V_{cold}}\right)KS t\right], \quad (4)$$

where  $\rho$ ,  $c$ ,  $V$  and  $S$  are density, heat capacity, volume and contact area, respectively. Here,  $S$  is estimate as the surface area of hexagonal cells dividing a bundle of SWNTs. Note that we have reduced a bundle of 7 SWNTs to a two body problem by assuming the homogeneous non-stationary heat transfer to the 6 surrounding SWNTs from the central one. The excellent agreement to an exponential fit by Eq. (3) in Fig. 13 shows the validity of the current analysis. Comparing Eq. (3) with Eq. (4), the thermal boundary conductance  $K$  was estimated to be about 4.04 MW/m<sup>2</sup>K.

Thermal boundary conductance between a nanotube and surrounding fluids or solids in various systems are being explored by molecular dynamics simulations. Through these simulations, we are trying to probe the physics of thermal boundary conductance, which is confined in atomic-scale

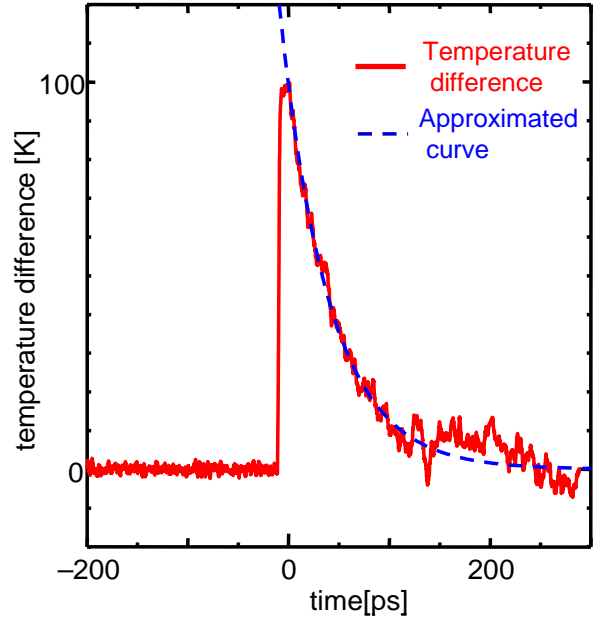


Fig. 13. Time history of the temperature difference of central and surrounding SWNTs.

layers adjacent to the SWNT and strongly dependent on their local properties. Contributions of the elastic and inelastic scatterings on the thermal boundary conductance and its dependence on the matrix phase have been quantified by analyzing the vibrational spectra.

## ACKNOWLEDGMENTS

Part of this work was financially supported by Grant-in-Aid for Scientific Research (22226006 and 19054003) from the Japan Society for the Promotion of Science, 'Development of Nanoelectronic Device Technology' of NEDO, and Global COE Program 'Global Center for Excellence for Mechanical Systems Innovation', MEXT, Japan.

## REFERENCES

1. S. Iijima, T. Ichihashi, Nature 363, 603 (1993).
2. K. S. Novoselov, A. K. Geim, S. V. Morozov, D. Jiang, M. I. Katsnelson, I. V. Grigorieva, S. V. Dubonos, A. A. Firsov, Nature 438, 197 (2005).
3. A. Jorio, G. Dresselhaus, M. S. Dresselhaus, M. S. Carbon Nanotubes: AdVanced Topics in the Synthesis, Structure, Properties and Applications (Topics in Applied Physics); Springer: New York, (2008).
4. S. Maruyama, R. Kojima, Y. Miyauchi, S. Chiashi, M. Kohno, Chem. Phys. Lett. 360, 229 (2002).
5. Y. Murakami, S. Chiashi, Y. Miyauchi, M. H. Hu, M. Ogura, T. Okubo, S. Maruyama, Chem. Phys. Lett. 385, 298 (2004).
6. K. Hata, D. N. Futaba, K. Mizuno, T. Namai, M. Yumura, S. Iijima, Science 306, 1362 (2004).

7. G. Y. Zhang, D. Mann, L. Zhang, A. Javey, Y. M. Li, E. Yenilmez, Q. Wang, J. P. McVittie, Y. Nishi, J. Gibbons, H. J. Dai, *Proc. Natl. Acad. Sci. U.S.A.* 102, 16141 (2005).
8. G. F. Zhong, T. Iwasaki, K. Honda, Y. Furukawa, I. Ohdomari, H. Kawarada, *Jpn. J. Appl. Phys.* 44, 1558 (2005).
9. G. Eres, A. A. Kinkhabwala, H. Cui, D. B. Geohegan, A. A. Puzos, D. H. Lowndes, *J. Phys. Chem. B* 109, 16684 (2005).
10. Y. Murakami, Y. Miyauchi, S. Chiashi, S. Maruyama, *Chem. Phys. Lett.* 377, 49 (2003).
11. S. Noda, H. Sugime, T. Osawa, Y. Tsuji, S. Chiashi, Y. Murakami, S. Maruyama, *Carbon* 44, 1414 (2006).
12. H. Sugime, S. Noda, S. Maruyama, Y. Yamaguchi, *Carbon* 47, 234 (2009).
13. M. H. Hu, Y. Murakami, M. Ogura, S. Maruyama, T. Okubo, *J. Catal.* 225, 230 (2004).
14. R. Xiang, E. Einarsson, H. Okabe, S. Chiashi, J. Shiomi, S. Maruyama, *Jpn. J. Appl. Phys.*, 49, 02BA03 (2010).
15. R. Xiang, T. Wu, E. Einarsson, Y. Suzuki, Y. Murakami, J. Shiomi, S. Maruyama, *J. Am. Chem. Soc.*, 131-30, 10344 (2009).
16. H. Oshima, Y. Suzuki, T. Shimazu, S. Maruyama, *Jpn. J. Appl. Phys.* 47, 1982 (2007).
17. R. Xiang, E. Einarsson, J. Okawa, Y. Miyauchi, S. Maruyama, *J. Phys. Chem. C*, 113, 7511 (2009).
18. S. Maruyama, E. Einarsson, Y. Murakami, T. Edamura, *Chem. Phys. Lett.* 403, 320 (2005).
19. E. Einarsson, M. Kadowaki, K. Ogura, J. Okawa, R. Xiang, Z. Zhang, Y. Yamamoto, Y. Ikuhara, S. Maruyama, *J. Nanosci. Nanotechnol.* 8, 6093 (2008).
20. E. Einarsson, Y. Murakami, M. Kadowaki, S. Maruyama, *Carbon* 46, 923 (2008).
21. R. Xiang, E. Einarsson, J. Okawa, T. Thurakitseree, Y. Murakami, J. Shiomi, Y. Ohno, S. Maruyama, *J. Nanosci. Nanotech.*, 10, 3901 (2010).
22. R. Xiang, Z. Zhang, K. Ogura, J. Okawa, E. Einarsson, Y. Miyauchi, J. Shiomi, S. Maruyama, *Jpn. J. Appl. Phys.* 47, 1971 (2008).
23. E. Einarsson, H. Shiozawa, C. Kramberger, M. H. Rummeli, A. Gruneis, T. Pichler, S. Maruyama, *J. Phys. Chem. C* 111, 17861 (2007).
24. Y. Murakami and S. Maruyama, *Chem. Phys. Lett.*, 422, 575 (2006).
25. P. T. Araujo, S. K. Doorn, S. Kilina, S. Tretiak, E. Einarsson, S. Maruyama, H. Chacham, M. A. Pimenta, A. Jorio, *Phys. Rev. Lett.*, 98, 067401 (2007).
26. H. M. Duong, D. V. Papavassiliou, K. J. Mullen and S. Maruyama, *J. Phys. Chem. C*, 112, 19860 (2008).
27. Y. Miyauchi, M. Oba and S. Maruyama, *Phys. Rev. B*, 74-20, 205440 (2006).
28. Z. Zhang, E. Einarsson, Y. Murakami, Y. Miyauchi and S. Maruyama, *Phys. Rev. B*, 81, 165442 (2010).
29. R. Andrews, D. Jacques, D. Qian, T. Rantell, *Acc. Chem. Res.* 35, 1008 (2002).
30. E. R. Meshot, A. J. Hart, *Appl. Phys. Lett.* 92, 113107 (2008).
31. D. B. Geohegan, A. A. Puzos, I. N. Ivanov, S. Jesse, G. Eres, J. Y. Howe, *Appl. Phys. Lett.* 83, 1851 (2003).
32. A. Ulman, *Chemical Reviews* 96, 1533 (1996).
33. S. Maruyama, T. Kimura, *Therm. Sci. Eng.* 7, 63 (1999).
34. S. Berber, Y-K. Kwon and D. Tomanek, *Phys. Rev. Lett.* 84, 4613 (2000).
35. J. Hone, M.C. Llaguno, M. J. Biercuk, A.T. Johnson, B. Batlogg, Z. Benes, J. E. Fischer, *Appl. Phys. A* 74, 339 (2002).
36. P. Kim, L. Shi, A. Majumdar, and P. L. McEuen, *Phys. Rev. Lett.* 87, 215502 (2001).
37. M. Fujii, X. Zhang, H. Xie, H. Ago, K. Takahashi, T. Ikuta, H. Abe and T. Shimizu, *Phys. Rev. Lett.* 95, 065502 (2005).
38. C. Yu, L. Shi, Z. Yao, D. Li and A. Majumdar, *Nano Lett.* 5, 1842 (2005).
39. E. Pop, D. Mann, Q. Wang, K. Goodson and H. Dai 6, 96 (2006).
40. G. Chen, *Nanoscale Energy Transport and Conversion*, Oxford University Press, New York (2005).
41. S. Maruyama, *Physica B*, 323, 193 (2002).
42. S. Maruyama, *Micro. Therm. Eng.*, 7, 41 (2003).
43. R. Livi and S. Lepri, *Nature*, 421, 327 (2003).
44. N. Mingo and D. A. Broido, *Nano Lett.* 5, 1221 (2005).
45. J. Wang and J-S Wang, *Appl. Phys. Lett.* 88, 111909 (2006).
46. D. W Brenner, *Phys. Rev. B*, 42, 9458 (1990).
47. Y. Yamaguchi and S. Maruyama, S., *Chem. Phys. Lett.*, 286, 336 (1998).
48. J. Hone, M. Whitney, C. Piskoti, A. Zettl, *Phys. Rev. B* 59, R2514 (1999).
49. T. Yamamoto, S. Watanabe, K. Watanabe, *Phys. Rev. Lett.* 92, 075502 (2004).
50. J. Shiomi, S. Maruyama, *Jpn. J. Appl. Phys.*, 47, 2005(2008).
51. J. Shiomi, S. Maruyama, *Phys. Rev. B*, 73, 205420 (2006).
52. R. Saito, G. Dresselhaus and M. S. Dresselhaus, *Physical Properties of Carbon Nanotubes*, Imperial College Press, London (1998).
53. G. D. Mahan and G. S. Jeon, *Phys. Rev. B*, 70, 075405 (2004).
54. T. Yamamoto, S. Konabe, J. Shiomi and S. Maruyama, *Appl. Phys. Express*, 2-9, 095003 (2009).
55. C. W. Chang, D. Okawa, H. Garcia, A. Majumdar, and A. Zettl, *Phys. Rev. Lett.* 101, 075903 (2008).
56. J. Shiomi, S. Maruyama, *Phys. Rev. B*, 74, 155401 (2006).
57. M. J. Biercuk, M. C. Llaguno, M. Radosavljevic, J. K. Hyun, A. T. Johnson, J. E. Fischer, *Appl. Phys. Lett.* 80, 2767 (2002).

58. S. U. S. Choi, Z. G. Zhang, W. Yu, F. E. Lockwood, E. A. Grulke, *Appl. Phys. Lett.* 79, 2252 (2001).
59. S. T. Huxtable, D. G. Cahill, S. Shenogin, L. Xue, R. Ozisik, P. Barone, M. Usrey, M. S. Strano, G. Siddons, M. Shim, P. Keblinski, *Nature Materials* 2, 731 (2003).
60. S. Shenogin, L. Xue, R. Ozisik, P. Keblinski, D. G. Cahill, *J. Appl. Phys.* 95, 8136 (2004).
61. H. M. Duong, N. Yamamoto, K. Bui, D. V. Papavassiliou, S. Maruyama, B. L. Wardle, *J. Phys. Chem. C*, 114, 8851, (2010).
62. H. M. Duong, D. V. Papavassiliou, K. J. Mullen, B. L. Wardle, S. Maruyama, *Int. J. Heat Mass Transf.*, 52, 5591, (2009).
63. H. M. Duong, N. Yamamoto, D. V. Papavassiliou, S. Maruyama, B. L. Wardle, *Nanotechnology*, 20, 155702, (2009).
64. H. M. Duong, D. V. Papavassiliou, K. J. Mullen, S. Maruyama, *J. Phys. Chem. C*, 112-50, 19860, (2008).
65. S. Maruyama, Y. Igarashi, Y. Taniguchi, J. Shiomi, *J. Therm. Sci. Tech.*, 1, 138 (2006).
66. C. F. Carlborg, J. Shiomi, and S. Maruyama, *Phys. Rev. B* 78 (2008) 205406.